









A Near-IR Search for Helium in the Superluminous Supernova SN 2024ahr

HARSH KUMAR ^{1,2} EDO BERGER ^{1,2} PETER K. BLANCHARD ^{1,2} SEBASTIAN GOMEZ ¹ DAICHI HIRAMATSU ^{1,2}
MOIRA ANDREWS,³ K. AZALEE BOSTROEM,³ YIZE DONG ^{1,4} JOSEPH FARAH,^{3,5} ESTEFANIA PADILLA GONZALEZ,^{3,5}
D. ANDREW HOWELL,^{3,5} CURTIS McCULLY,³ DARSHANA MEHTA ⁴ MEGAN NEWSOME,^{3,5} ARAVIND P. RAVI ⁴ AND
GIACOMO TERRERAN³

¹Center for Astrophysics | Harvard & Smithsonian, 60 Garden Street, Cambridge, MA 02138-1516, USA

²The NSF AI Institute for Artificial Intelligence and Fundamental Interactions, USA

³Las Cumbres Observatory, 6740 Cortona Drive, Suite 102, Goleta, CA 93117-5575, USA

⁴Department of Physics and Astronomy, University of California, 1 Shields Avenue, Davis, CA 95616-5270, USA

⁵Department of Physics, University of California, Santa Barbara, CA 93106-9530, USA

ABSTRACT

We present a detailed study of SN 2024ahr, a hydrogen-poor superluminous supernova (SLSN-I), for which we determine a redshift of $z = 0.0861$. SN 2024ahr has a peak absolute magnitude of $M_g \approx M_r \approx -21$ mag, rest-frame rise and decline times (50% of peak) of about 40 and 80 days, respectively, and typical spectroscopic evolution in the optical band. Similarly, modeling of the UV/optical light curves with a magnetar spin-down engine leads to typical parameters: an initial spin period of ≈ 3.3 ms, a magnetic field strength of $\approx 6 \times 10^{13}$ G, and an ejecta mass of $\approx 9.5 M_\odot$. Due to its relatively low redshift we obtained a high signal-to-noise ratio near-IR spectrum about 43 rest-frame days post-peak to search for the presence of helium. We do not detect any significant feature at the location of the He I $\lambda 2.058 \mu\text{m}$ feature, and place a conservative upper limit of $\sim 0.05 M_\odot$ on the mass of helium in the outer ejecta. We detect broad features of Mg I $\lambda 1.575 \mu\text{m}$ and a blend of Co II $\lambda 2.126 \mu\text{m}$ and Mg II $\lambda 2.136 \mu\text{m}$, which are typical of Type Ic SNe, but with higher velocities. Examining the sample of SLSNe-I with NIR spectroscopy, we find that, unlike SN 2024ahr, these events are generally peculiar. This highlights the need for a large sample of prototypical SLSNe-I with NIR spectroscopy to constrain the fraction of progenitors with helium (Ib-like) and without helium (Ic-like) at the time of explosion, and hence the evolutionary path(s) leading to the rare outcome of SLSNe-I.

Keywords: Supernovae() — Optical astronomy() — Transient() — NIR Spectroscopy() — Astronomical spectroscopy()

1. INTRODUCTION

Modern wide-field optical time-domain surveys have enabled the discovery of a rare class of transients dubbed “hydrogen poor superluminous supernovae” (SLSNe-I), which can exceed the luminosities of normal stripped-envelope core-collapse Supernovae (Type Ib and Ic SNe) by two orders of magnitude (Quimby et al. 2007; Gal-Yam et al. 2009; Barbary et al. 2009; Quimby et al. 2011; Chomiuk et al. 2011; Gal-Yam 2012; Sukhbold & Woosley 2016; Gal-Yam 2019a; Nicholl 2021; Gomez et al. 2024). SLSNe-I also exhibit systematically longer timescales and bluer colors at an early time and distinct optical/UV spectra near peak and in the nebular phase compared to normal SNe Ib/c (Mazzali et al. 2016; Smith et al. 2018; Gal-Yam 2019b). Taken together, these properties point to a different power source in SLSNe-I, namely a highly magnetized, rapidly spinning neutron star (magnetar; Kasen & Bildsten 2010; Woosley 2010), as opposed to radioactive decay of ^{56}Ni in normal SNe Ib/c. In addition, SLSNe-I are rare ($\lesssim 0.3\%$ of SESNe (type Ib/c) Quimby et al. 2013; Frohmaier et al. 2021), exhibit a distinct pre-explosion mass distribution (Blanchard et al. 2020), and occur in different host galaxy and local environments than SNe Ib/c (Chen et al. 2015; Perley et al. 2016), pointing to a restricted evolutionary path to their formation.

Although there are substantial differences between SLSNe-I and SNe Ib/c, both types of explosions arise from stripped massive stars, and it is therefore natural to explore whether SLSNe-I also exhibits a sub-class that is Ib-like (retaining a helium layer) or if these events are only Ic-like (stripped of helium). The presence of helium can in principle

be probed in the optical regime, using He I lines at 3888, 5875, 6678, and 7065 Å (Matheson et al. 2001; Gerardy et al. 2002; Yan et al. 2020), but these lines tend to be blended with other, stronger features (e.g., Ca II λ 3934, 3968Å, Na I λ 5875 – 5890Å, and C II λ 6580, 7234Å), especially in the case of SLSNe-I, which have large ejecta velocities and hence broad features. Additionally, the optical lines are expected to be weak and may thus be present only for large helium shell masses ($\gtrsim 0.2 - 1.0 M_{\odot}$; Teffs et al. 2020). Taken together, this limits claims of helium detections in the optical band from being robust (Yan et al. 2020).

On the other hand, as shown in the case of SNe Ib/c, NIR spectroscopy provides a more robust probe for the presence of helium (Holmbo et al. 2023). In particular, the two strongest He I lines in the NIR are at 1.083 and 2.058 μm , with a third weaker line at 1.700 μm . However, as in the optical band, the 1.083 μm line suffers from blending with C I and Mg II, and it is therefore present in both SNe Ib and Ic, even if the latter lack helium (Shahbandeh et al. 2022). The 2.058 μm line, however, is free of strong blending and thus provides the most robust signature for helium (e.g., Matheson et al. 2001; Williamson et al. 2021; Shahbandeh et al. 2022). Indeed, models of SNe Ib/c spectra have shown that even a nearly bare CO core, with a helium mass down to $\sim 0.1 M_{\odot}$, can still lead to a detectable signature at 2.058 μm (Hachinger et al. 2012; Teffs et al. 2020).

Only a few attempts have been made to obtain NIR spectra of SLSNe-I covering the He I λ 2.058 μm line, predominantly in the nearest events (SN 2017egm: Zhu et al. 2023; SN 2018bsz: Pursiainen et al. 2022; SN 2018ibb: Schulze et al. 2024; and SN 2019hge: Chen et al. 2023. SN 2019hge). These NIR searches resulted predominantly in non-detection, with the single exception of a claimed detection in SN 2019hge at $z = 0.0866$ (Yan et al. 2020); we note that this event is one of the lowest luminosity SLSNe-I detected to date, comparable to the luminous end of normal SESNe (Gomez et al. 2022).

Here, we present a detailed study of the relatively nearby ($z \approx 0.08$) SLSN-I event SN 2024ahr, including NIR spectroscopy to search for the presence of helium. We demonstrate that SN 2024ahr is typical of the luminous SLSN-I population, and show that its NIR spectrum is similar to a SN Ic (albeit with broader features). The paper is arranged as follows. In §2 we present the discovery of SN 2024ahr and our UV, optical, and NIR follow-up observations. In §3 we explore the photometric properties and model the light curves with a magnetar central engine model; discuss the spectroscopic evolution; and analyze the NIR spectrum, including a comparison to the small sample of existing NIR spectra of SLSNe-I, and determination of a limit on the helium mass. We summarize the key results in §4.

2. DISCOVERY AND OBSERVATIONS

2.1. Discovery and Classification

SN 2024ahr was discovered by the Zwicky Transient Facility (ZTF; Bellm 2014; Bellm et al. 2019) on 2024 January 16 (MJD = 60325), with an internal designation ZTF24aacrbua. It was also detected by ATLAS (ATLAS24bwz), Pan-STARRS (PS24aun), Gaia (Gaia24apk), and BlackGem (BGEM J142159.27–123021.9) independently¹. The discovery magnitude was $m_g = 20.98 \pm 0.33$, with a position of R.A.=00^h24^m34.71^s, Decl.=+47°13′21.″55 (J2000) (Fremling 2024). Images of SN 2024ahr from our follow-up observations and its underlying host galaxy from archival Pan-STARRS DR2 are shown in Figure 1.

Wise et al. (2024) obtained a spectrum of SN 2024ahr on 2024 March 6 (50 days post-discovery), and classified it as a SLSN-I at an approximate redshift of $z \approx 0.1$, based on template matches to previous SLSNe-I. Here we refine the redshift to $z = 0.08612 \pm 0.00004$ based on host-galaxy emission lines.

2.2. Optical Imaging Observations

Las Cumbres Observatory (LCO)—We conducted follow-up imaging observations with the Sinistro cameras on the 1-meter telescopes in the Las Cumbres Observatory (LCO; Brown et al. 2013) network starting on 2024 March 8 to September 15 (192 days) The observations were part of the Global Supernova Project (Howell & Global Supernova Project 2017a) and utilized the B, V, g, r, i filters. Photometric measurements were made using the point-spread function (PSF) fitting, employing the `lco_gtsnpipeline` pipeline (Valenti et al. 2016). The g, r, i images were processed with the ZOGY image subtraction algorithm (Zackay et al. 2016) using PanSTARRS DR2 image as templates. In the absence of reference templates in B and V bands, we report the PSF photometry. Given the blue color of the galaxy and the brightness of the source, we do not expect the lack of image subtraction to affect the photometry significantly in these bands.

¹ <https://www.wis-tns.org/object/2024ahr/>

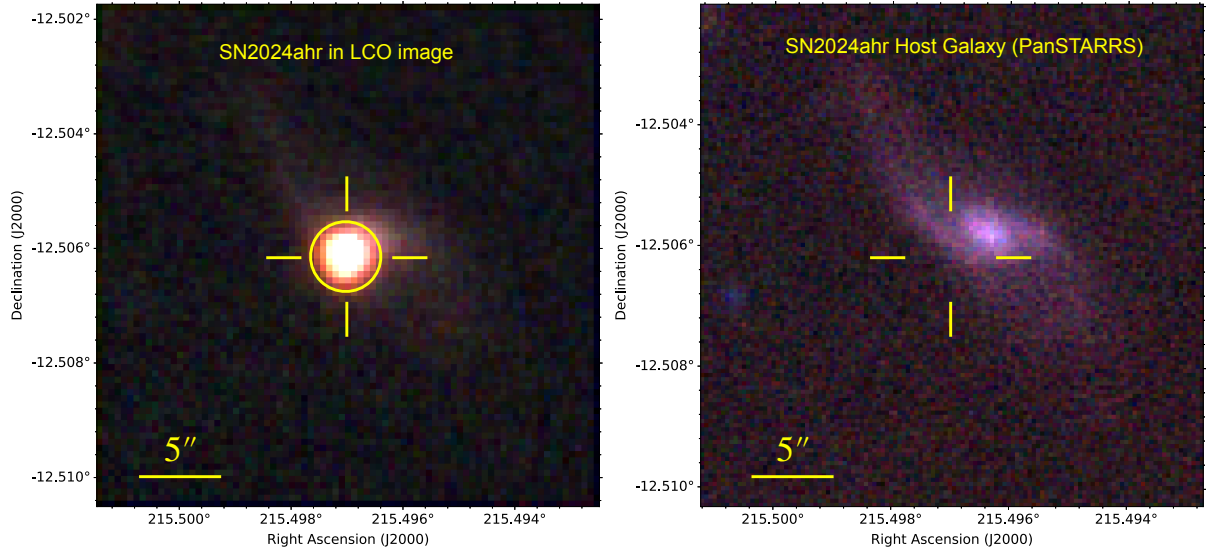


Figure 1. *Left:* RGB image of SN 2024ahr from our Las Cumbres Observatory data, about 59 days after discovery (yellow circle). *Right:* Pre-discovery image of the host galaxy from PanSTARRS-DR2 data (Flewelling 2018). SN 2024ahr is located $\approx 2.45''$ (≈ 4.1 kpc) from the center of the host galaxy near a spiral arm.

Zwicky Transient Facility (ZTF)—The ZTF observations cover the time range from discovery on 2024 January 16 to July 28 (195 days) in the g, r bands. We obtained the ZTF photometry from the Automatic Learning for the Rapid Classification of Events (ALeRCE) broker (Förster et al. 2021).

Asteroid Terrestrial-impact Last Alert System (ATLAS)—The ATLAS observations cover the time range from 2024 January 16 to July 28 (195 days) in the c band and from 2024 January 15 to August 2 (201 days) in the o -band. We obtained ATLAS photometry through the ATLAS Forced Photometry Server (Shingles et al. 2021), selecting data with a signal-to-noise ratio of ≥ 5 .

Neil Gehrels Swift Observatory—We obtained ultraviolet and optical observations using the UV/Optical Telescope (UVOT; Roming et al. 2005) in six filters (UVW2, UVM2, UVW1, U , B , V) in several epochs spanning from 2024 April 4 to August 3 (123 days). We performed aperture photometry using the UVOTSOURCE pipeline with an aperture of $5''$ radius, and included standard aperture corrections. We used a signal-to-noise ratio of ≥ 5 as the detection limit in all bands. Since the transient was still bright when the field became Sun-constrained, no template images are available for image subtraction. Therefore, the photometry at later epochs (MJD > 60450) in the UV filters is probably contaminated by host emission and is excluded from the subsequent analysis.

The light curves of SN 2024ahr are shown in Figure 2. Photometric measurements in the g, c, r, i , and o bands are in AB magnitudes, and all other photometry is in the Vega system unless stated otherwise. All measurements have been corrected for Galactic extinction, with $E(B - V) = 0.092$ mag (Schlafly & Finkbeiner 2011), assuming the Fitzpatrick (1999) reddening law with $R_V = 3.1$. Throughout this work, we use standard Planck18 FlatLambdaCDM cosmology (Planck Collaboration et al. 2020) with Hubble constant $H_0 = 67.4 \pm 0.5$ km s $^{-1}$ Mpc $^{-1}$; matter density parameter $\Omega_m = 0.315 \pm 0.007$. We estimated a luminosity distance of $d_L = 405 \pm 19$ Mpc using a redshift $z = 0.08612 \pm 0.00004$ (see § 2.3) for SN 2024ahr.

2.3. Optical Spectroscopy

Following the SLSN-I classification of SN 2024ahr, we obtained 6 epochs of LCO optical spectra with the FLOYDS spectrographs mounted on the 2m Faulkes Telescope North (FTN) and South (FTS) at Haleakala (USA) and Siding Spring (Australia), respectively, spanning from 2024 March 9 to May 14. The observations were made as a part of the Global Supernova Project (Howell & Global Supernova Project 2017b). We used a $2''$ slit placed on the target along

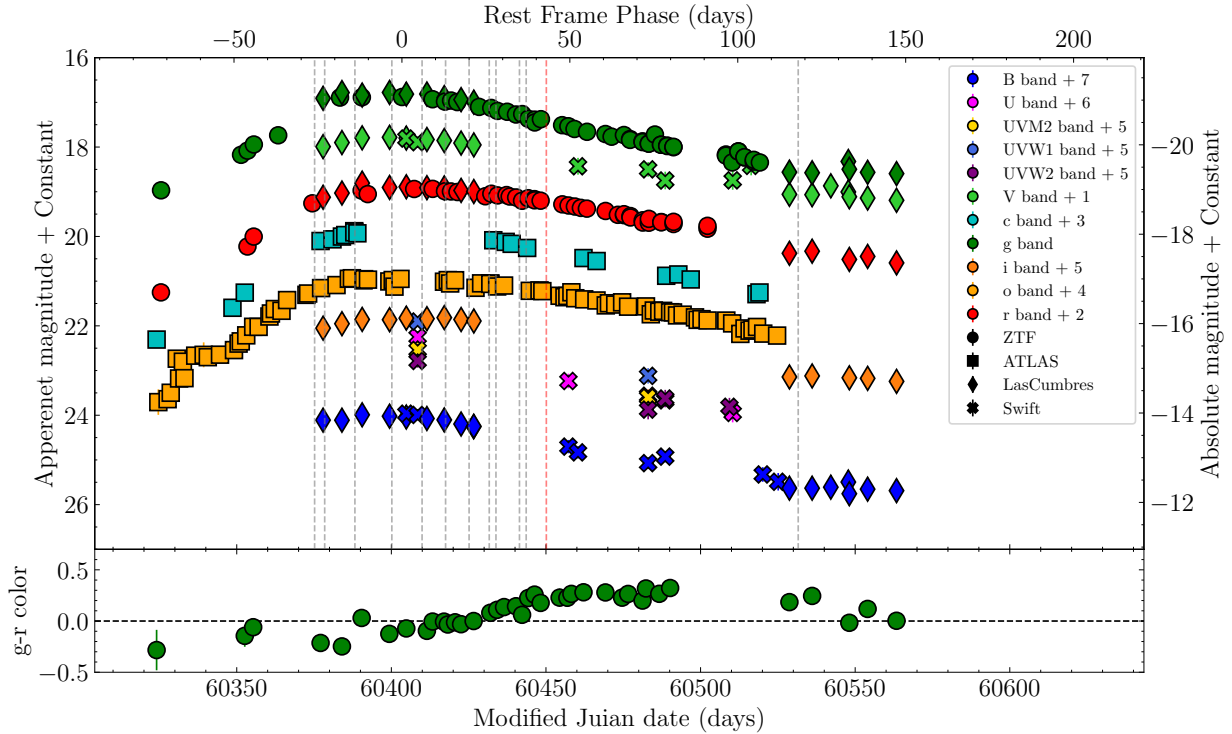


Figure 2. Optical and UV light curves of SN 2024ahr. All magnitudes are plotted in AB system and are corrected for Galactic Extinction. Vertical lines mark the epochs of optical (gray lines) and NIR (red line) spectroscopy. SN 2024ahr rises from discovery to peak in ≈ 78 d and reaches a peak absolute magnitude of $m_g \approx m_r \approx -21.0$. The $g - r$ color (bottom) gradually reddens from about -0.3 to $+0.3$ mag from the rise to the decline of the light curve. The o -band light curve shows an early bump.

the parallactic angle (Filippenko 1982). One-dimensional spectra were extracted, reduced, and calibrated following standard procedures using `floyds_pipeline`² (Valenti et al. 2014). The resulting spectra are plotted in Figure 3.

We also obtained a spectrum as a part of follow-up observations on 2024 May 1 with the Low-Resolution Imaging Spectrometer (LRIS; Oke et al. 1995) mounted on the Keck I 10-m telescope. The observations were performed with a $1''$ wide slit, the 600/4000 grism, 400/8500 grating, and a 560 dichroic setup. The data were reduced using standard procedures in the fully-automated reduction pipeline for LRIS longslit spectra, `LPipe` (Perley 2019). The spectrum covers a wavelength range of $3824 - 9197 \text{ \AA}$ with a resolution of ≈ 1500 .

We obtained an additional spectrum with the Binospec spectrograph (Fabricant et al. 2019) on the 6.5-m MMT telescope on 2024 May 11. We used a combination of 270 lines/mm grating with $1''$ wide slit and the LP3800 filter, covering a wavelength range of $3825 - 9200 \text{ \AA}$ with a resolution of ≈ 1500 . The data was reduced using `PyRAF` following standard procedure via the MMT pipeline. The one-dimensional spectrum was extracted and flux-calibrated using standard star observation obtained at the same configuration close in time to the science observations.

Finally, we obtained a spectrum using the Low Dispersion Survey Spectrograph 3 (LDSS3; Stevenson et al. 2016) on the 6.5-m Magellan Clay telescope on 2024 August 9. We used the VPH-All grism with a $1''$ wide slit, covering a wavelength range of $4264 - 9652 \text{ \AA}$ with a resolution of ≈ 700 . The spectrum was bias-subtracted and flat-fielded, and the sky background was modeled and subtracted from the 2D image. The one-dimensional spectra were extracted, and a wavelength calibration was applied using an arc lamp spectrum taken directly after the science image. Relative flux calibration was applied using standard star observation obtained at the same configuration close in time to the science observations.

The spectra (see Figure 3) exhibit multiple host galaxy emission lines ($H\alpha$, $H\beta$, $H\gamma$, $[N \text{ II}]$, $[O \text{ II}]$, $[O \text{ III}]$ and $[Na \text{ I D}]$) from which we determine a redshift of $z = 0.08612 \pm 0.00004$.

² https://github.com/LCOGT/floyds_pipeline

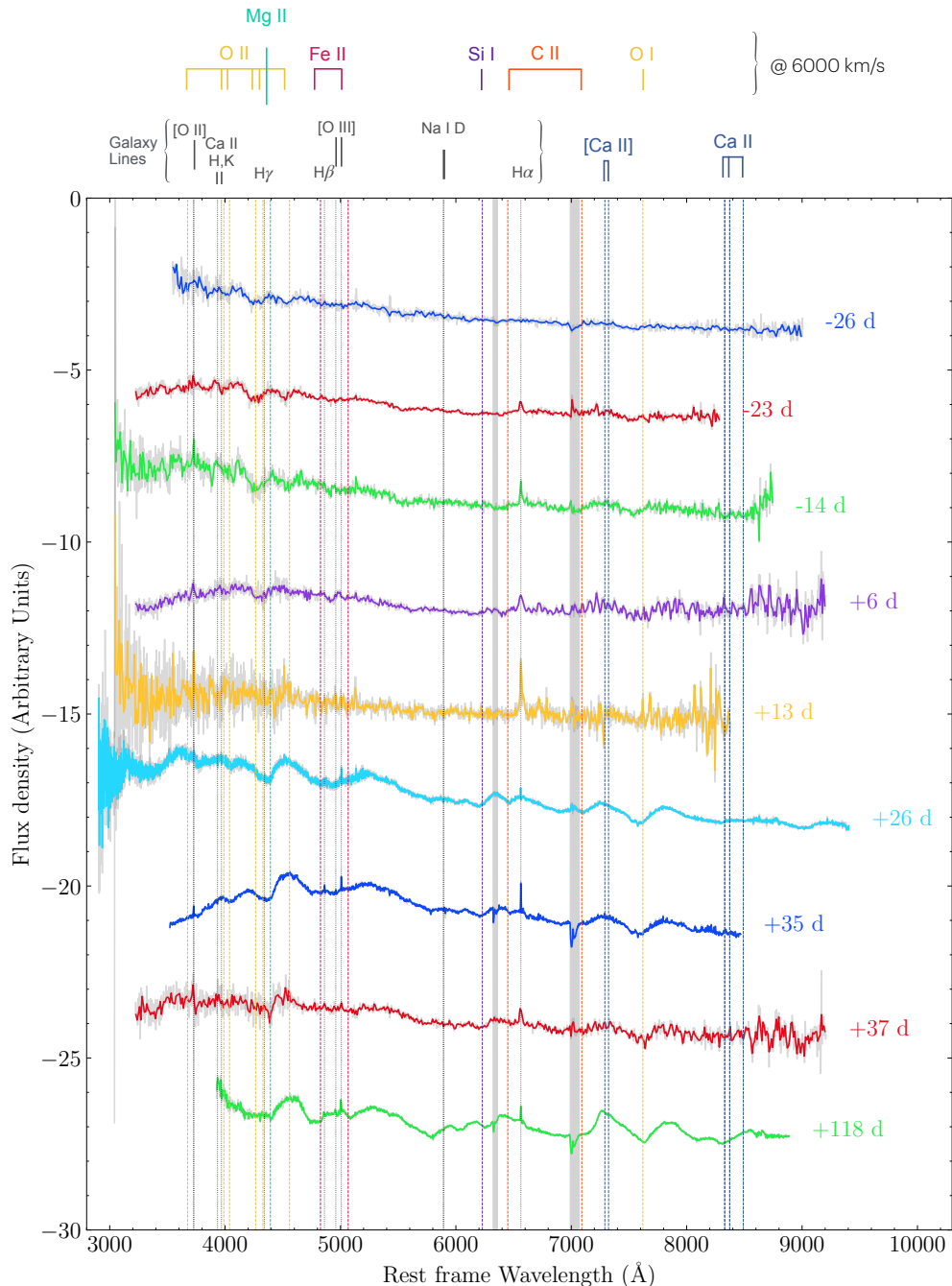


Figure 3. Optical spectra of SN 2024ahr, spanning phases of -26 to $+118$ d. The spectra exhibit a blue continuum at early time with O II and Fe II/Fe III lines typical of SLSNe-I. At later times, the spectra are dominated by various ionization states of O, Fe, C, and Ca with a typical velocity of ~ 6000 km s^{-1} . The blueshifted position of features is marked with $v = 6000$ km s^{-1} estimated using the spectrum at $+35$ d.

2.4. Near-IR Spectroscopy

Given the relatively low redshift of SN 2024ahr, we initiated a search for helium lines by obtaining a NIR spectrum with the FLAMINGOS-2 spectrograph on the Gemini-South 8-m telescope on 2024 May 20 through a Director's Discretionary Time (DDT) program (GS-2024A-DD-106, PI: Kumar). We used the HK Filter and disperser pair with a focal plane mask of the 3-pixel slit (0.45) at low read-noise to obtain multiple science exposures totaling about

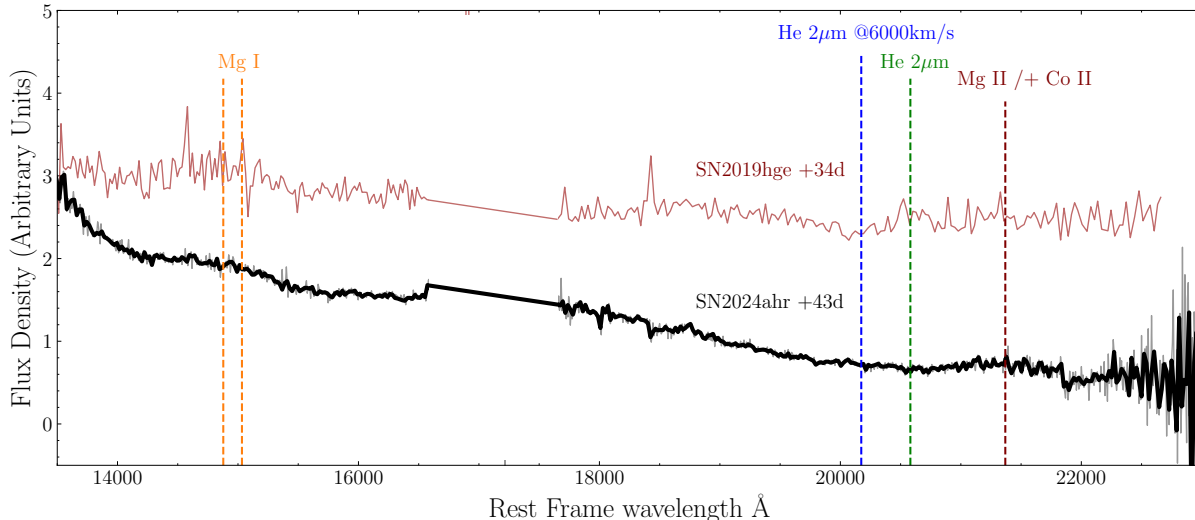


Figure 4. NIR spectrum of SN 2024ahr obtained at a phase of +43 d (black). The Spectrum exhibits broad features of Mg I ($\sim 1.5 \mu\text{m}$) and Mg II + Co II ($\sim 2.13 \mu\text{m}$). We do not detect significant absorption from He I at $2\mu\text{m}$. For comparison, we also show the NIR spectrum of SN 2019hge (brown), which appears to exhibit the He I $\lambda 2.058 \mu\text{m}$ line with a blueshift of $\approx 6000 \text{ km s}^{-1}$ (Yan et al. 2020).

2 hours on the source. The slit was aligned to the parallactic angle to minimize atmospheric dispersion. The HK grating provides coverage at $1.45 - 2.45 \mu\text{m}$. We reduced the data using the `PyPeIt` package (Prochaska et al. 2020). The spectral images were flat-fielded using `GCALflats` to correct pixel-to-pixel sensitivity variations. Wavelength calibration was achieved using OH sky emission lines that are well-distributed across the NIR range. A flux calibration was applied using a sensitivity function estimated from two nearby A0V standard stars. The resulting 1D spectra were co-added, and the spectrum was corrected for telluric absorption. The resulting spectrum is plotted in Figure 4.

3. ANALYSIS

3.1. Photometric Evolution and Light Curve Modeling

The UV and optical light curves of SN 2024ahr are plotted in Figure 2. The light curve of SN 2024ahr is characterized by a gradual rise from discovery to a peak of $m_g \approx 17.1 \text{ mag}$ ($M_g \approx -21$) on 2024 April 3 (MJD = 60403.425, which we define as phase = 0 d), over a span of 78 days. After the peak, the light curve shows a shallow decline, reaching half brightness in g -band over 80 days. During the rising phase, the $g - r$ color gradually reddens from ≈ -0.3 at discovery to ≈ 0.0 at peak and then further reddens to ≈ 0.3 at a phase of +100 days in the observed frame. The light curve evolution of SN 2024ahr is typical of the SLSNe-I population (Gomez et al. 2024). Assuming a blackbody SED, we estimate a temperature of $\approx 10,500 \text{ K}$ and a photospheric radius of $\approx 4 \times 10^{15} \text{ cm}$ at the peak of the light curve.

In the initial 20 days after discovery, SN 2024ahr exhibits a clear “bump”, about 2 mag fainter than the mean peak in the high-cadence ATLAS α -band data. Such bumps have been observed in some previous SLSNe-I (Nicholl & Smartt 2016; Angus et al. 2019), and the relative brightness of the SN 2024ahr bump to its peak brightness is comparable to previous events. Such bumps have been speculated to arise from the shock breakout emission driven by the central engine in pre-expanded ejecta or due to interaction with a dense circumstellar medium confined in proximity to the progenitor. Given the paucity of data at other bands during this bump, we cannot determine its origin in detail.

We model the light curves of SN 2024ahr using the Modular Open-Source Fitter for Transients `MOSFiT` (Guillochon et al. 2017) `s1snni` model, following the approach and priors used in the large population study of Nicholl et al. (2017) and Gomez et al. (2024). We use a Gaussian prior on the ejecta velocity of $\sim 10^4 \text{ km s}^{-1}$ based on the spectra. We used 200 MCMC walkers with 20,000 steps to ensure a thorough exploration of the parameter space and confirmed convergence using the Gelman-Rubin statistic, ensuring that all chains had a potential scale reduction factor below 1.2. We fit the multi-band light curves from phase -55 d onwards (i.e., neglecting the early-time bump, which the model cannot accommodate). We also remove the late-time UV photometry (UVW1, UVW2, UVM2) at phase $\geq 75 \text{ d}$ due to significant host contamination. The best-fit model light curves are shown in Figure 5, providing a good

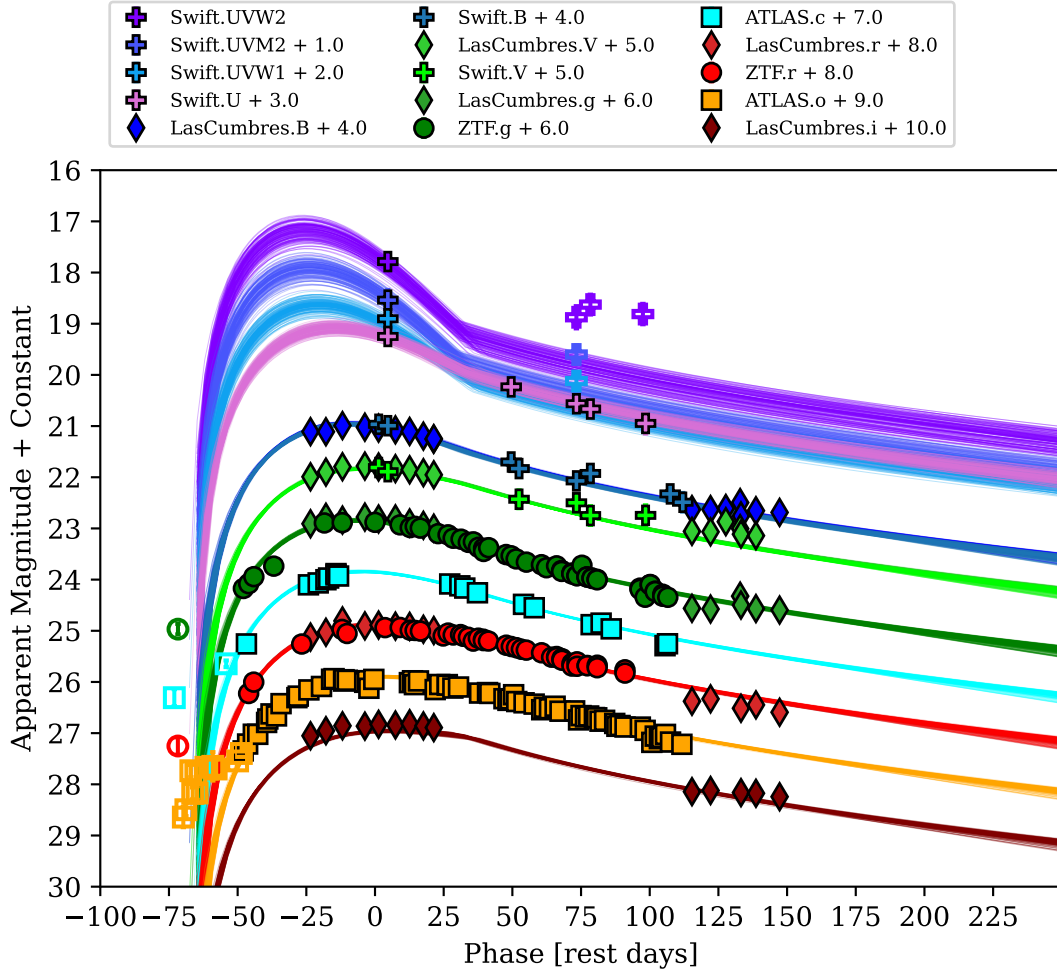


Figure 5. Multi-band MOSFiT model light curves for SN 2024ahr. The model provides an excellent fit to the data over a span of about 200 days. The data points shown with open markers are not used in the fit (early bump, and UV points contaminated by host galaxy emission).

match to the observed optical/UV light curves over a span of about 200 days. The posteriors of the model parameters are listed in Table 1, and are typical of the SLSN population: $P_{\text{spin}} \approx 3.3$ ms, $B \approx 5 \times 10^{13}$ G, and $M_{\text{ej}} \approx 10 M_{\odot}$.

3.2. Optical Spectral Evolution and Local Metallicity

We present the optical spectral evolution of SN 2024ahr in Figure 3. The spectra before the peak are dominated by a blue continuum, with broad, weak absorption features of O II with a blueshift velocity of ≈ 9746 km s^{-1} (measured at phase = -26 d). In the near-peak phase, Fe II + Mg II features starts to emerge at $\approx 4400 \text{ \AA}$. In addition, the O $\lambda 7774$ absorption feature starts to appear at the peak phase. We measure a velocity of ≈ 7700 km s^{-1} in near-peak (phase = +6 d). In the post-peak phase, O II and Fe II/ Mg II absorption features start to weaken yet, remain present, and the O $\lambda 7774$ feature gets stronger and becomes evident with a velocity of 6812 km s^{-1} (at phase = +35d). Furthermore, Si II $\lambda 6355$, C II $\lambda 6580$ and $\lambda 7234$ and O I $\lambda 7774$ features emerge and become stronger over time. In the near-nebular phase (+118 d), we see the potential emergence of [O I] $\lambda \lambda 6300, 6364$ features, [Ca II] $\lambda \lambda 7291, 7323$ emission lines and likely emissions from Ca II NIR triplet around 8500 \AA . The spectral features seen in SN 2024ahr spectrum are typical of SLSNe-I.

We detect a few host galaxy lines in the SN 2024ahr spectra. The $H\alpha$, $H\beta$, $H\gamma$, Na I D and [O III] lines from the host are clearly visible in $\lambda 4500\text{-}\lambda 7000$ region of the spectra. We also detect Ca II H, K lines at the rest wavelengths representing the Ca lines from the host. We use the host galaxy emission lines from the +35 d spectrum ($H\alpha$, $H\beta$, $H\gamma$, [O II] and [O III]) to determine the metallicity at the location of SN 2024ahr, using the R23 diagnostic Pagel et al.

Table 1. Parameter Posterior Values of the `s1snni` Model from MOSFiT.

Parameter	Prior	Posterior
P_{spin} (ms)	Uniform	$3.32^{+0.30}_{-0.29}$
B ($\times 10^{14}$ G)	log	$0.56^{+0.43}_{-0.11}$
M_{ej} (M_{\odot})	Uniform	$9.51^{+3.24}_{-2.55}$
v_{ej} ($\times 10^3$ km s $^{-1}$)	log	$5.0^{+5.0}_{-2.5}$
t_{exp} (days)	Uniform	$-19.5^{+0.9}_{-0.8}$
$\log f_{\text{Ni}}$	log	$-2.0^{+0.6}_{-0.7}$
$\log n_{\text{H,host}}$	log	$20.8^{+0.1}_{-0.2}$
λ_{cutoff} (\AA)	Uniform	3468^{+199}_{-240}
α	Uniform	$1.76^{+0.44}_{-0.39}$
T_{min} (K)	Uniform	9510^{+328}_{-449}
M_{NS} (M_{\odot})	Uniform	$1.71^{+0.17}_{-0.16}$
θ_{PB}	Uniform	$0.93^{+0.49}_{-0.47}$
$\log \sigma$	log	$-1.13^{+0.02}_{-0.02}$

(1979); Kobulnicky et al. (1999); Nagao et al. (2006). We used $12 + \log(\text{O}/\text{H}) - [\text{N II}]\lambda 6584/\text{H}\alpha$ and $12 + \log(\text{O}/\text{H}) - [\text{O III}]\lambda 5007/[\text{N II}]\lambda 6584$ metallicity correlations to estimate $12 + \log(\text{O}/\text{H}) = 8.55 \pm 0.05$ and 8.64 ± 0.09 respectively. Both correlations rule out the lower R23 metallicity branch (Nagao et al. 2006). The value of $12 + \log(\text{O}/\text{H}) \approx 8.6$ is consistent with the range for SLSNe-I (Lunnan et al. 2014; Cleland et al. 2023).

3.3. NIR Spectroscopic Analysis

The NIR spectrum of SN 2024ahr shown in Figure 4 exhibits two broad features at $\approx 1.5\mu\text{m}$ and $\approx 2.1\mu\text{m}$. We identify the $1.5\mu\text{m}$ feature as Mg I $\lambda 1.575\mu\text{m}$, and the $2.1\mu\text{m}$ feature as a blend of Mg II $\lambda 2.136\mu\text{m}$ and Co II $\lambda 2.126\mu\text{m}$; both sets of features are seen in stripped-envelope SNe, Type Ib and Ic (Shahbandeh et al. 2022). We do not find clear evidence for the He I $\lambda 2.058\mu\text{m}$ feature. We compare our spectrum to that of SN 2019hge, which is the only SLSN-I to date that shows potential signs of helium in its NIR spectrum (Yan et al. 2020). The spectrum of SN 2019hge shows a more convincing feature of He I. with a blueshift of about 6000 km s^{-1} , as well as a potential signature of Mg I $\lambda 1.575\mu\text{m}$, but it does not clearly exhibit the Mg II/Co II blend.

A comparison of our SN 2024ahr NIR spectrum with all publicly available NIR spectra of SLSNe-I at the nearest available rest-frame phase is shown in Figure 6. With the exception of SN 2019hge, none of the other SLSNe-I show the presence of He I $\lambda 2.058\mu\text{m}$, or evidence for Mg I or the Mg II/Co II blend. We note that the previous events are mostly atypical of the general SLSN-I population: SN 2019hge and SN 2018bsz are at the low luminosity end of the population ($M_r \approx -19.6$ mag; Yan et al. 2020); SN 2018ibb is a claimed pair-instability SN candidate (Schulze et al. 2024); and SN 2017egm has a claimed helium detection from optical spectra and the $1\mu\text{m}$ line (Zhu et al. 2023), but exhibits no clear detection of the $2\mu\text{m}$ line, which suggests that the previous claim is due to blending with other lines.

Also shown in Figure 6 is a comparison with the NIR spectra of typical SNe Ib and Ic at a similar phase. The comparison shows that SN 2024ahr is more analogous to a SN Ic, exhibiting Mg I and Mg II/Co II, but with higher velocities, while being distinguished from a SN Ib by lacking the clear He I $\lambda 2.058\mu\text{m}$ line.

To assess a limit on the mass of helium in the outer layers of the ejecta from the lack of He I $\lambda 2.058\mu\text{m}$ detection, we model the spectrum of SN 2024ahr using the TARDIS code (Kerzendorf & Sim 2014), which provides rapid spectral modeling using parameters such as composition, density profile, velocity, luminosity, and temperature as input. We use a model similar to that presented in Williamson et al. (2021) with the luminosity, ejecta mass, velocity, temperature, density, and abundances adjusted to match the photometric and spectroscopic properties of SN 2024ahr. We then add varying amounts of helium (0, 0.025, and 0.05 M_{\odot}) to the outer layers of the ejecta to estimate the amount of helium that can be present in SN 2024ahr at the time of our NIR spectrum.

A comparison of our SN 2024ahr spectrum to the TARDIS synthetic spectra around the location of the He I $\lambda 2.058\mu\text{m}$ line is shown in Figure 7. The model provides an overall good fit to the observed spectrum, including the observed feature due to Mg II/Co II. We find that a helium mass of $\sim 0.05 M_{\odot}$ would have produced a notable absorption

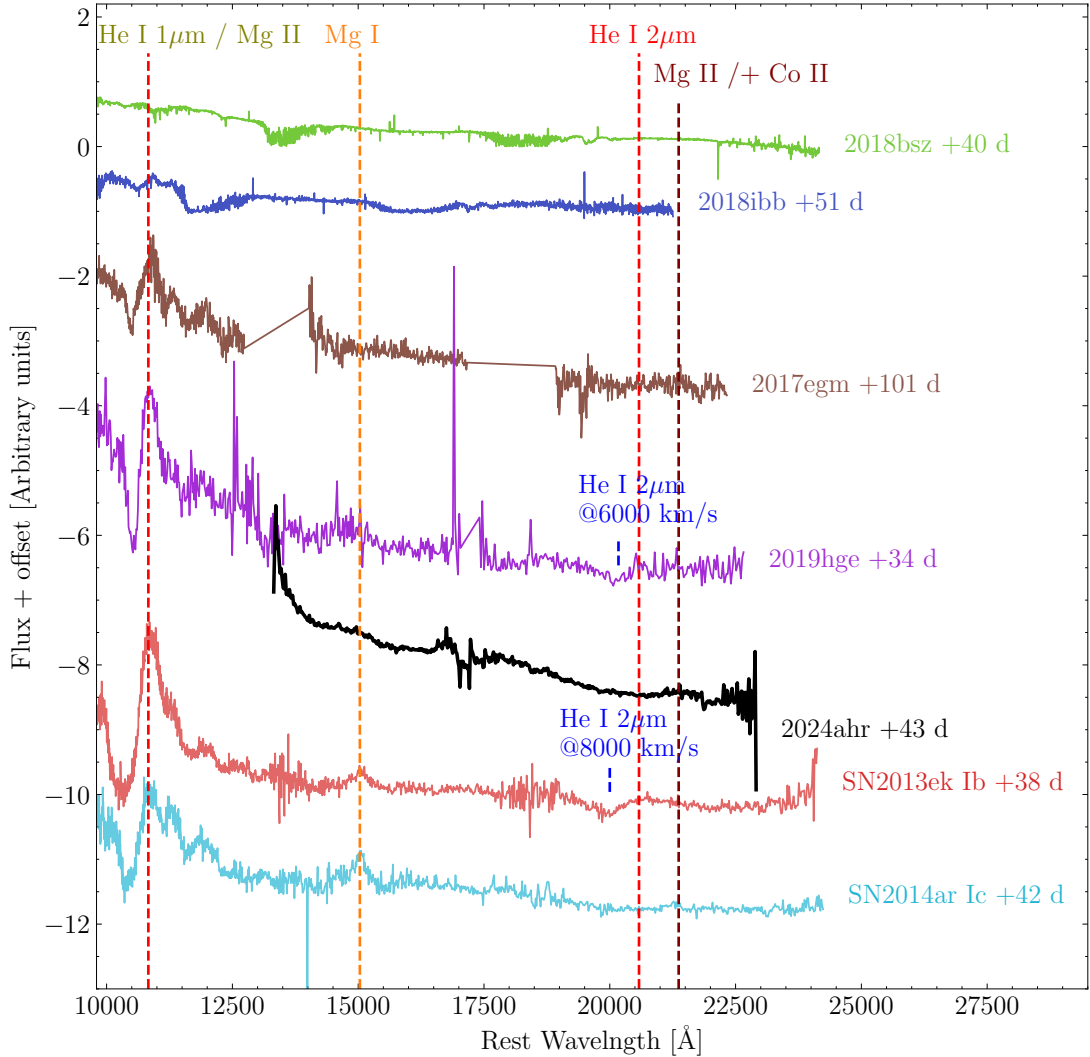


Figure 6. NIR spectral comparison of SN 2024ahr with all publicly available NIR spectra of SLSNe-I at a similar phase. We identify detections of Mg I at $\approx 1.5\mu\text{m}$ and Mg II, Co II feature at $\approx 2.1\mu\text{m}$. All comparison SLSNe-I, except for SN2019hge, do not show any detection of the He I $2\mu\text{m}$ feature in their NIR spectra. Data obtained from Yan et al. (2020); Pursiainen et al. (2022); Shahbandeh et al. (2022); Zhu et al. (2023); Schulze et al. (2024).

feature that is not present in the data, and we therefore use this value as a conservative upper limit on the helium mass in the outer ejecta layers of SN 2024ahr.

4. CONCLUSIONS

We presented detailed photometric and spectroscopic observations of the SLSN-I SN 2024ahr, and determined its precise redshift to $z = 0.0861$, making it one of the nearest SLSN-I to date. The optical/UV light curves, optical spectra, and inferred model parameters of SN 2024ahr are all typical of the SLSN-I population, and specifically with the median peak absolute magnitude of ~ -21 .

Taking advantage of the low redshift, we obtained a high signal-to-noise ratio NIR spectrum to robustly explore for presence of helium via the He I $\lambda 2.058\mu\text{m}$ line. The spectrum reveals broad features of Mg I, Mg II + Co II which are typical of Type Ic SNe, but with higher expansion velocities. We do not detect absorption at the location of the He I $\lambda 2.058\mu\text{m}$ line, and using spectral modeling, we place a rough upper limit of $\sim 0.05 M_{\odot}$ on the mass of helium present in the outer ejecta. This suggests that the progenitor of SN 2024ahr was stripped of both hydrogen and helium (i.e., Ic-like). Detailed NIR ground-based spectroscopy in progress will determine whether any other SLSNe-I

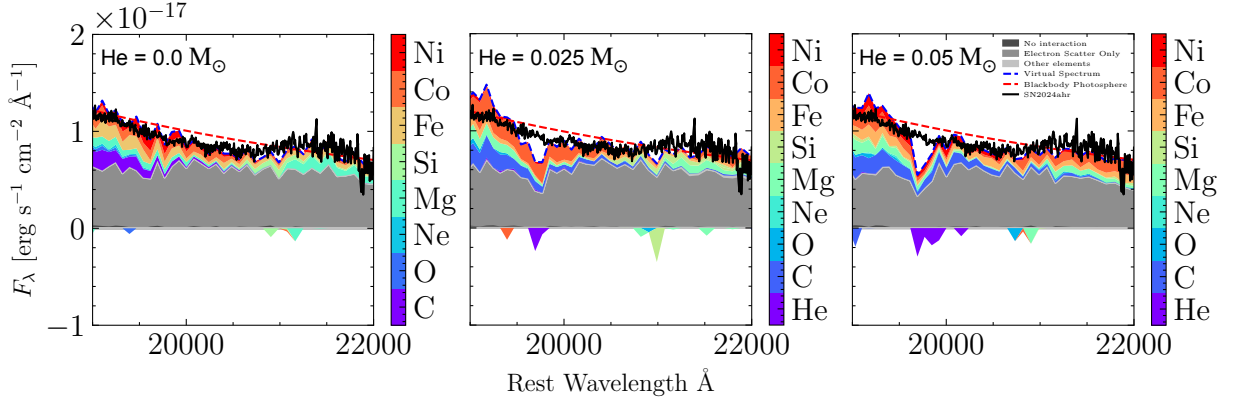


Figure 7. TARDIS model spectra with helium masses of 0, 0.025, and 0.05 M_{\odot} , compared to our spectrum of SN 2024ahr near the He I $\lambda 2.058 \mu\text{m}$ line. The contribution of various element is represented by different colors labeled in the color bar. We find that a helium mass of 0.05 M_{\odot} would have produced a notable absorption feature in the spectrum, and use this value as a rough upper limit on the helium mass in the outer layers of the ejecta.

at $z \lesssim 0.1$ exhibit robust evidence for helium, and future observations with JWST will provide such insight over a broader redshift range and to fainter magnitudes.

We are grateful to Kali Salmas, Alejandra Milone and Benjamin Weiner for scheduling the MMT Binospec observations and Yuri Beletsky for performing the Magellan LDSS-3 observations.

The Berger Time-Domain research group at Harvard is supported by the NSF and NASA grants. The LCO supernova group is supported by NSF grants AST-1911151 and AST-1911225.

Observations reported here were obtained at the MMT Observatory, a joint facility of the Smithsonian Institution and the University of Arizona. This paper uses data products produced by the OIR Telescope Data Center, supported by the Smithsonian Astrophysical Observatory. This work makes use of observations from the Las Cumbres Observatory global telescope network. The authors wish to recognize and acknowledge the very significant cultural role and reverence that the summit of Haleakalā has always had within the indigenous Hawaiian community. We are most fortunate to have the opportunity to conduct observations from the mountain.

We thank the support of the staff at the Neil Gehrels Swift Observatory.

This research made use of `PypeIt`,³ a Python package for semi-automated reduction of astronomical slit-based spectroscopy (Prochaska et al. 2020; Prochaska et al. 2020).

This work has made use of data from the Zwicky Transient Facility (ZTF). ZTF is supported by NSF grant No. AST-1440341 and a collaboration including Caltech, IPAC, the Weizmann Institute for Science, the Oskar Klein Center at Stockholm University, the University of Maryland, the University of Washington, Deutsches Elektronen-Synchrotron and Humboldt University, Los Alamos National Laboratories, the TANGO Consortium of Taiwan, the University of Wisconsin–Milwaukee, and Lawrence Berkeley National Laboratories. Operations are conducted by COO, IPAC, and UW. The ZTF forced-photometry service was funded under the Heising-Simons Foundation grant No. 12540303 (PI: Graham).

This work has made use of data from the Asteroid Terrestrial-impact Last Alert System (ATLAS) project. The Asteroid Terrestrial-impact Last Alert System (ATLAS) project is primarily funded to search for near-earth asteroids through NASA grants NN12AR55G, 80NSSC18K0284, and 80NSSC18K1575; byproducts of the NEO search include images and catalogs from the survey area. This work was partially funded by Kepler/K2 grant J1944/80NSSC19K0112 and HST GO-15889, and STFC grants ST/T000198/1 and ST/S006109/1. The ATLAS science products have been made possible through the contributions of the University of Hawaii Institute for Astronomy, the Queen’s University Belfast, the Space Telescope Science Institute, the South African Astronomical Observatory, and The Millennium Institute of Astrophysics (MAS), Chile. This research made use of TARDIS, a community-developed software package for spectral synthesis in supernovae (Kerzendorf & Sim 2014; Kerzendorf et al. 2024). The development of TARDIS received support from GitHub, the Google Summer of Code initiative, and from ESA’s Summer of Code in Space program. TARDIS is a fiscally sponsored project of NumFOCUS. TARDIS makes extensive use of Astropy and Pyne.

This research has made use of the NASA Astrophysics Data System (ADS), the NASA/IPAC Extragalactic Database (NED), and NASA/IPAC Infrared Science Archive (IRSA, which is funded by NASA and operated by the California Institute of Technology) and IRAF (which is distributed by the National Optical Astronomy Observatory, NOAO, operated by the Association of Universities for Research in Astronomy, AURA, Inc., under cooperative agreement with the NSF).

TNS is supported by funding from the Weizmann Institute of Science, as well as grants from the Israeli Institute for Advanced Studies and the European Union via ERC grant No. 725161.

Facilities: ATLAS, LCO, Swift(XRT and UVOT) and ZTF, MMT

Software: `astropy` (Astropy Collaboration et al. 2013, 2018, 2022), `SExtractor` (Bertin & Arnouts 1996) `NumPy` (Oliphant 2015), `photutils` (Bradley et al. 2022), `PyRAF` (Science Software Branch at STScI 2012), `SciPy` (Virtanen et al. 2020) and `MOSFiT` (Guillochon et al. 2017)

APPENDIX

A. PHOTOMETRY

MJD	Filter	Mag System	Magnitude \pm e_magnitude (AB)	Telescope
60324.08414	c	AB	19.31 ± 0.17	ATLAS
60324.63717	o	AB	$> 19.71 \pm 0.28$	ATLAS
60325.48944	r	AB	19.25 ± 0.17	ZTF
60325.52751	g	AB	18.97 ± 0.10	ZTF
60327.64583	o	AB	19.64 ± 0.2	ATLAS
60328.65230	o	AB	19.5 ± 0.12	ATLAS
60330.61142	o	AB	18.73 ± 0.13	ATLAS
60331.35503	o	AB	19.18 ± 0.12	ATLAS
60332.58525	o	AB	$> 18.8 \pm 0.23$	ATLAS
60333.09649	o	AB	19.17 ± 0.13	ATLAS
60336.57452	o	AB	18.67 ± 0.17	ATLAS
60339.30233	o	AB	$> 18.65 \pm 0.28$	ATLAS
60340.63145	o	AB	18.7 ± 0.19	ATLAS
60344.58362	o	AB	18.64 ± 0.07	ATLAS
60348.61786	c	AB	18.6 ± 0.06	ATLAS
60349.11079	o	AB	18.54 ± 0.06	ATLAS
60350.59033	o	AB	18.4 ± 0.05	ATLAS
60351.30575	o	AB	18.35 ± 0.05	ATLAS
60351.40104	g	AB	18.17 ± 0.08	ZTF
60352.59256	c	AB	18.26 ± 0.04	ATLAS
60353.07085	o	AB	18.21 ± 0.04	ATLAS
60353.46939	r	AB	18.23 ± 0.080	ZTF
60353.50177	g	AB	18.08 ± 0.080	ZTF
60355.31720	o	AB	18.02 ± 0.04	ATLAS
60355.47949	r	AB	18.0 ± 0.070	ZTF
60355.52082	g	AB	17.94 ± 0.05	ZTF
60357.06662	o	AB	18.02 ± 0.03	ATLAS
60360.57107	o	AB	17.79 ± 0.040	ATLAS
60361.05397	o	AB	17.72 ± 0.03	ATLAS
60362.31309	o	AB	17.62 ± 0.05	ATLAS
60363.40083	g	AB	17.74 ± 0.15	ZTF
60364.47799	o	AB	17.66 ± 0.12	ATLAS
60366.28186	o	AB	17.42 ± 0.05	ATLAS
60372.54168	o	AB	17.31 ± 0.03	ATLAS
60373.08527	o	AB	17.28 ± 0.09	ATLAS
60374.45652	r	AB	17.26 ± 0.05	ZTF
60377.11317	c	AB	17.1 ± 0.02	ATLAS
60377.28392	o	AB	17.16 ± 0.02	ATLAS
60377.92168	B	Vega	17.11 ± 0.01	LasCumbres
60377.92451	V	Vega	16.99 ± 0.02	LasCumbres
60377.92642	g	AB	16.91 ± 0.02	LasCumbres
60377.92924	r	AB	17.12 ± 0.02	LasCumbres
60377.93117	i	AB	17.05 ± 0.03	LasCumbres
60380.96319	c	AB	17.06 ± 0.02	ATLAS

60382.26828	o	AB	17.09 ± 0.02	ATLAS
60383.39547	g	AB	16.89 ± 0.06	ZTF
60384.01817	B	Vega	17.11 ± 0.02	LasCumbres
60384.02100	V	Vega	16.9 ± 0.02	LasCumbres
60384.02122	c	AB	17.0 ± 0.020	ATLAS
60384.02290	g	AB	16.78 ± 0.02	LasCumbres
60384.02576	r	AB	17.03 ± 0.02	LasCumbres
60384.02767	i	AB	16.95 ± 0.02	LasCumbres
60385.08850	c	AB	16.97 ± 0.01	ATLAS
60386.25692	o	AB	16.95 ± 0.02	ATLAS
60387.24077	o	AB	16.93 ± 0.02	ATLAS
60387.99893	c	AB	16.88 ± 0.03	ATLAS
60388.01445	c	AB	16.91 ± 0.02	ATLAS
60389.01396	c	AB	16.93 ± 0.02	ATLAS
60390.39617	r	AB	16.97 ± 0.040	ZTF
60390.46168	g	AB	16.89 ± 0.040	ZTF
60390.55718	B	Vega	16.99 ± 0.02	LasCumbres
60390.56002	V	Vega	16.79 ± 0.02	LasCumbres
60390.56196	g	AB	16.84 ± 0.01	LasCumbres
60390.56481	r	AB	16.81 ± 0.02	LasCumbres
60390.56674	i	AB	16.86 ± 0.02	LasCumbres
60390.99709	o	AB	16.98 ± 0.02	ATLAS
60391.17561	o	AB	16.96 ± 0.02	ATLAS
60392.36505	r	AB	17.05 ± 0.120	ZTF
60392.43633	o	AB	16.97 ± 0.04	ATLAS
60399.35003	o	AB	17.01 ± 0.02	ATLAS
60399.42088	B	Vega	17.02 ± 0.02	LasCumbres
60399.42371	V	Vega	16.78 ± 0.03	LasCumbres
60399.42561	g	AB	16.78 ± 0.02	LasCumbres
60399.42842	r	AB	16.9 ± 0.03	LasCumbres
60399.43035	i	AB	16.86 ± 0.04	LasCumbres
60400.44570	o	AB	16.97 ± 0.020	ATLAS
60401.00885	o	AB	17.12 ± 0.08	ATLAS
60402.95293	o	AB	16.95 ± 0.01	ATLAS
60403.42513	g	AB	16.88 ± 0.040	ZTF
60404.83115	B	Vega	17.04 ± 0.02	LasCumbres
60404.83401	V	Vega	16.8 ± 0.02	LasCumbres
60404.83596	g	AB	16.82 ± 0.02	LasCumbres
60404.83882	r	AB	16.89 ± 0.02	LasCumbres
60404.84073	i	AB	16.83 ± 0.02	LasCumbres
60404.87142	B	Vega	16.97 ± 0.070	Swift
60404.87947	V	Vega	16.81 ± 0.09	Swift
60407.38877	r	AB	16.94 ± 0.050	ZTF
60408.49503	UVW1	Vega	16.9 ± 0.12	Swift
60408.49590	U	Vega	16.25 ± 0.09	Swift
60408.49677	B	Vega	16.99 ± 0.09	Swift
60408.50012	UVW2	Vega	17.79 ± 0.15	Swift
60408.50100	V	Vega	16.89 ± 0.13	Swift
60408.50279	UVM2	Vega	17.54 ± 0.21	Swift
60411.49318	B	Vega	17.07 ± 0.01	LasCumbres

60411.49605	V	Vega	16.83 ± 0.02	LasCumbres
60411.49802	g	AB	16.81 ± 0.01	LasCumbres
60411.50088	r	AB	16.91 ± 0.02	LasCumbres
60411.50284	i	AB	16.84 ± 0.02	LasCumbres
60413.33685	g	AB	16.93 ± 0.040	ZTF
60413.37721	r	AB	16.94 ± 0.030	ZTF
60417.02692	o	AB	17.01 ± 0.02	ATLAS
60417.11246	B	Vega	17.1 ± 0.02	LasCumbres
60417.11529	V	Vega	16.85 ± 0.02	LasCumbres
60417.11721	g	AB	16.89 ± 0.02	LasCumbres
60417.12007	r	AB	16.91 ± 0.02	LasCumbres
60417.12196	i	AB	16.82 ± 0.03	LasCumbres
60417.35166	g	AB	16.98 ± 0.040	ZTF
60417.35888	r	AB	16.99 ± 0.040	ZTF
60418.25190	o	AB	16.98 ± 0.02	ATLAS
60419.01736	o	AB	17.05 ± 0.03	ATLAS
60419.26964	r	AB	16.99 ± 0.040	ZTF
60419.31528	g	AB	16.96 ± 0.03	ZTF
60420.60103	o	AB	16.98 ± 0.02	ATLAS
60421.32247	g	AB	16.99 ± 0.040	ZTF
60421.38245	r	AB	17.01 ± 0.05	ZTF
60422.55031	B	Vega	17.2 ± 0.02	LasCumbres
60422.55317	V	Vega	16.91 ± 0.02	LasCumbres
60422.55512	g	AB	16.94 ± 0.02	LasCumbres
60422.55800	r	AB	16.97 ± 0.02	LasCumbres
60422.55997	i	AB	16.86 ± 0.02	LasCumbres
60426.60778	B	Vega	17.26 ± 0.03	LasCumbres
60426.66139	B	Vega	17.25 ± 0.02	LasCumbres
60426.66561	V	Vega	16.95 ± 0.02	LasCumbres
60426.66754	g	AB	16.99 ± 0.02	LasCumbres
60426.67038	r	AB	16.99 ± 0.02	LasCumbres
60426.67228	i	AB	16.89 ± 0.03	LasCumbres
60427.21691	o	AB	17.15 ± 0.07	ATLAS
60428.38228	g	AB	17.1 ± 0.050	ZTF
60429.03034	o	AB	17.05 ± 0.02	ATLAS
60430.38148	r	AB	17.1 ± 0.05	ZTF
60431.99050	o	AB	17.05 ± 0.02	ATLAS
60432.00598	o	AB	17.06 ± 0.05	ATLAS
60432.31221	g	AB	17.13 ± 0.040	ZTF
60432.33711	r	AB	17.04 ± 0.06	ZTF
60432.96333	c	AB	17.09 ± 0.02	ATLAS
60434.21322	o	AB	17.12 ± 0.02	ATLAS
60434.33249	g	AB	17.19 ± 0.03	ZTF
60434.33771	r	AB	17.08 ± 0.040	ZTF
60436.44816	o	AB	17.1 ± 0.02	ATLAS
60436.96603	c	AB	17.12 ± 0.02	ATLAS
60437.25648	r	AB	17.07 ± 0.04	ZTF
60437.44613	g	AB	17.21 ± 0.060	ZTF
60438.26602	r	AB	17.11 ± 0.050	ZTF
60438.92011	c	AB	17.17 ± 0.02	ATLAS

60440.31531	g	AB	17.27 ± 0.040	ZTF
60440.36323	r	AB	17.13 ± 0.040	ZTF
60442.27101	r	AB	17.2 ± 0.03	ZTF
60442.31830	g	AB	17.26 ± 0.030	ZTF
60443.92262	c	AB	17.26 ± 0.02	ATLAS
60444.27338	r	AB	17.14 ± 0.050	ZTF
60444.32509	g	AB	17.37 ± 0.050	ZTF
60444.76937	o	AB	17.22 ± 0.04	ATLAS
60446.30615	r	AB	17.17 ± 0.05	ZTF
60446.30615	r	AB	17.19 ± 0.02	ZTF
60446.35646	g	AB	17.39 ± 0.050	ZTF
60446.35646	g	AB	17.45 ± 0.03	ZTF
60447.91065	o	AB	17.21 ± 0.03	ATLAS
60448.27046	r	AB	17.2 ± 0.050	ZTF
60448.36916	g	AB	17.38 ± 0.05	ZTF
60448.82955	o	AB	17.22 ± 0.030	ATLAS
60454.41774	o	AB	17.33 ± 0.05	ATLAS
60455.23133	g	AB	17.51 ± 0.040	ZTF
60455.29560	r	AB	17.28 ± 0.08	ZTF
60455.98819	o	AB	17.36 ± 0.04	ATLAS
60456.91827	o	AB	17.33 ± 0.020	ATLAS
60457.25102	g	AB	17.53 ± 0.040	ZTF
60457.26601	U	Vega	17.23 ± 0.16	Swift
60457.26655	B	Vega	17.7 ± 0.15	Swift
60457.31492	r	AB	17.31 ± 0.05	ZTF
60458.22738	o	AB	17.25 ± 0.03	ATLAS
60459.23141	g	AB	17.6 ± 0.05	ZTF
60459.35644	r	AB	17.33 ± 0.04	ZTF
60459.47113	o	AB	17.38 ± 0.05	ATLAS
60460.36116	B	Vega	17.83 ± 0.14	Swift
60460.36531	V	Vega	17.43 ± 0.19	Swift
60461.29211	r	AB	17.36 ± 0.040	ZTF
60462.13953	c	AB	17.48 ± 0.020	ATLAS
60462.35592	o	AB	17.41 ± 0.02	ATLAS
60463.23333	r	AB	17.38 ± 0.050	ZTF
60463.27476	g	AB	17.66 ± 0.05	ZTF
60466.34191	o	AB	17.43 ± 0.02	ATLAS
60466.37715	c	AB	17.55 ± 0.03	ATLAS
60469.22962	g	AB	17.71 ± 0.05	ZTF
60469.27388	r	AB	17.43 ± 0.040	ZTF
60469.33921	o	AB	17.54 ± 0.020	ATLAS
60470.36083	o	AB	17.49 ± 0.02	ATLAS
60471.22924	g	AB	17.77 ± 0.05	ZTF
60472.40384	o	AB	17.52 ± 0.03	ATLAS
60473.24841	r	AB	17.52 ± 0.050	ZTF
60474.62768	o	AB	17.47 ± 0.02	ATLAS
60475.21093	g	AB	17.73 ± 0.06	ZTF
60475.23213	r	AB	17.52 ± 0.050	ZTF
60475.23213	r	AB	17.5 ± 0.02	ZTF
60476.57139	o	AB	17.57 ± 0.03	ATLAS

60477.20998	g	AB	17.82 ± 0.07	ZTF
60477.20998	g	AB	17.84 ± 0.04	ZTF
60477.32791	r	AB	17.54 ± 0.070	ZTF
60477.32791	r	AB	17.58 ± 0.04	ZTF
60481.23105	g	AB	17.87 ± 0.08	ZTF
60481.23105	g	AB	17.89 ± 0.06	ZTF
60481.30275	r	AB	17.64 ± 0.07	ZTF
60481.30275	r	AB	17.69 ± 0.05	ZTF
60482.34075	o	AB	17.57 ± 0.050	ATLAS
60483.03957	UVW1	Vega	18.12 ± 0.17	Swift
60483.04061	U	Vega	17.56 ± 0.14	Swift
60483.04166	B	Vega	18.07 ± 0.13	Swift
60483.04671	UVW2	Vega	18.87 ± 0.22	Swift
60483.04776	V	Vega	17.5 ± 0.16	Swift
60483.05557	UVM2	Vega	18.6 ± 0.18	Swift
60483.24998	g	AB	17.92 ± 0.08	ZTF
60483.24998	g	AB	17.92 ± 0.06	ZTF
60483.27690	r	AB	17.69 ± 0.06	ZTF
60483.27690	r	AB	17.61 ± 0.03	ZTF
60483.90807	o	AB	17.74 ± 0.07	ATLAS
60484.88288	o	AB	17.66 ± 0.07	ATLAS
60485.23256	g	AB	17.72 ± 0.050	ZTF
60486.64395	o	AB	17.68 ± 0.03	ATLAS
60487.21367	g	AB	17.95 ± 0.06	ZTF
60487.21367	g	AB	17.95 ± 0.02	ZTF
60487.29531	r	AB	17.68 ± 0.06	ZTF
60487.29531	r	AB	17.68 ± 0.030	ZTF
60487.88439	o	AB	17.66 ± 0.03	ATLAS
60488.56850	U	Vega	17.67 ± 0.15	Swift
60488.56947	B	Vega	17.93 ± 0.13	Swift
60488.57408	UVW2	Vega	18.63 ± 0.19	Swift
60488.57505	V	Vega	17.75 ± 0.20	Swift
60488.88209	c	AB	17.88 ± 0.03	ATLAS
60489.21492	g	AB	17.97 ± 0.06	ZTF
60489.21492	g	AB	17.98 ± 0.030	ZTF
60490.15739	o	AB	17.7 ± 0.03	ATLAS
60491.07838	o	AB	17.7 ± 0.03	ATLAS
60491.22653	g	AB	18.0 ± 0.06	ZTF
60491.22653	g	AB	18.0 ± 0.03	ZTF
60491.25539	r	AB	17.72 ± 0.050	ZTF
60491.25539	r	AB	17.67 ± 0.02	ZTF
60492.38837	o	AB	17.77 ± 0.03	ATLAS
60492.81733	c	AB	17.85 ± 0.03	ATLAS
60494.19315	o	AB	17.75 ± 0.02	ATLAS
60496.80960	c	AB	17.96 ± 0.03	ATLAS
60498.19322	o	AB	17.81 ± 0.020	ATLAS
60499.05855	o	AB	17.87 ± 0.03	ATLAS
60500.30509	o	AB	17.85 ± 0.03	ATLAS
60502.24168	r	AB	17.83 ± 0.06	ZTF
60502.24168	r	AB	17.76 ± 0.03	ZTF

60502.27800	o	AB	17.88 ± 0.03	ATLAS
60508.20521	g	AB	18.17 ± 0.12	ZTF
60508.20521	g	AB	18.19 ± 0.09	ZTF
60508.32324	o	AB	17.88 ± 0.090	ATLAS
60509.33890	UVW2	Vega	18.81 ± 0.20	Swift
60510.21934	o	AB	17.95 ± 0.05	ATLAS
60510.22771	g	AB	18.34 ± 0.15	ZTF
60510.38450	U	Vega	17.95 ± 0.21	Swift
60510.39098	V	Vega	17.75 ± 0.21	Swift
60512.22896	g	AB	18.1 ± 0.14	ZTF
60512.22896	g	AB	18.1 ± 0.1	ZTF
60512.85743	o	AB	18.18 ± 0.09	ATLAS
60514.19013	g	AB	18.23 ± 0.10	ZTF
60514.19013	g	AB	18.23 ± 0.06	ZTF
60514.22316	o	AB	18.06 ± 0.08	ATLAS
60515.85070	o	AB	18.11 ± 0.08	ATLAS
60516.36757	V	Vega	17.42 ± 0.21	Swift
60516.79299	o	AB	18.08 ± 0.04	ATLAS
60517.19021	g	AB	18.33 ± 0.10	ZTF
60517.19021	g	AB	18.29 ± 0.06	ZTF
60518.08816	c	AB	18.29 ± 0.04	ATLAS
60518.26193	o	AB	18.02 ± 0.04	ATLAS
60519.05224	c	AB	18.25 ± 0.040	ATLAS
60519.17758	g	AB	18.34 ± 0.09	ZTF
60520.11622	B	Vega	18.33 ± 0.16	Swift
60520.26668	o	AB	18.17 ± 0.05	ATLAS
60524.75334	o	AB	18.22 ± 0.06	ATLAS
60525.10893	B	Vega	18.49 ± 0.20	Swift
60528.73356	B	Vega	18.63 ± 0.03	LasCumbres
60528.73637	V	Vega	18.06 ± 0.04	LasCumbres
60528.73825	g	AB	18.56 ± 0.04	LasCumbres
60528.74105	r	AB	18.38 ± 0.05	LasCumbres
60528.74294	i	AB	18.14 ± 0.07	LasCumbres
60536.07695	B	Vega	18.63 ± 0.05	LasCumbres
60536.07975	V	Vega	18.07 ± 0.04	LasCumbres
60536.08160	g	AB	18.58 ± 0.03	LasCumbres
60536.08439	r	AB	18.33 ± 0.03	LasCumbres
60536.08626	i	AB	18.12 ± 0.04	LasCumbres
60542.11852	B	Vega	18.61 ± 0.1	LasCumbres
60542.12159	V	Vega	17.87 ± 0.06	LasCumbres
60547.78241	B	Vega	18.49 ± 0.09	LasCumbres
60547.78544	V	Vega	18.0 ± 0.12	LasCumbres
60547.78753	g	AB	18.32 ± 0.04	LasCumbres
60548.10462	B	Vega	18.76 ± 0.05	LasCumbres
60548.10769	V	Vega	18.11 ± 0.03	LasCumbres
60548.10983	g	AB	18.5 ± 0.05	LasCumbres
60548.11288	r	AB	18.51 ± 0.04	LasCumbres
60548.11502	i	AB	18.16 ± 0.05	LasCumbres
60554.02099	B	Vega	18.65 ± 0.03	LasCumbres
60554.02400	V	Vega	18.14 ± 0.03	LasCumbres

60554.02609	g	AB	18.57 ± 0.03	LasCumbres
60554.02909	r	AB	18.45 ± 0.03	LasCumbres
60554.03115	i	AB	18.18 ± 0.05	LasCumbres
60563.37217	B	Vega	18.69 ± 0.06	LasCumbres
60563.37498	V	Vega	18.19 ± 0.05	LasCumbres
60563.37688	g	AB	18.59 ± 0.04	LasCumbres
60563.37970	r	AB	18.59 ± 0.03	LasCumbres
60563.38159	i	AB	18.24 ± 0.04	LasCumbres

Table 2. Photometry of SN 2024ahr. Magnitudes are corrected for Galactic Extinction in the direction of SN 2024ahr.

REFERENCES

- Angus, C. R., Smith, M., Sullivan, M., et al. 2019, *MNRAS*, 487, 2215, doi: [10.1093/mnras/stz1321](https://doi.org/10.1093/mnras/stz1321)
- Astropy Collaboration, Robitaille, T. P., Tollerud, E. J., et al. 2013, *A&A*, 558, A33, doi: [10.1051/0004-6361/201322068](https://doi.org/10.1051/0004-6361/201322068)
- Astropy Collaboration, Price-Whelan, A. M., Sipőcz, B. M., et al. 2018, *AJ*, 156, 123, doi: [10.3847/1538-3881/aabc4f](https://doi.org/10.3847/1538-3881/aabc4f)
- Astropy Collaboration, Price-Whelan, A. M., Lim, P. L., et al. 2022, *ApJ*, 935, 167, doi: [10.3847/1538-4357/ac7c74](https://doi.org/10.3847/1538-4357/ac7c74)
- Barbary, K., Dawson, K. S., Tokita, K., et al. 2009, *ApJ*, 690, 1358, doi: [10.1088/0004-637X/690/2/1358](https://doi.org/10.1088/0004-637X/690/2/1358)
- Bellm, E. 2014, in *The Third Hot-wiring the Transient Universe Workshop*, ed. P. R. Wozniak, M. J. Graham, A. A. Mahabal, & R. Seaman, 27–33, doi: [10.48550/arXiv.1410.8185](https://doi.org/10.48550/arXiv.1410.8185)
- Bellm, E. C., Kulkarni, S. R., Graham, M. J., et al. 2019, *PASP*, 131, 018002, doi: [10.1088/1538-3873/aaecbe](https://doi.org/10.1088/1538-3873/aaecbe)
- Bertin, E., & Arnouts, S. 1996, *A&AS*, 117, 393, doi: [10.1051/aas:1996164](https://doi.org/10.1051/aas:1996164)
- Blanchard, P. K., Berger, E., Nicholl, M., & Villar, V. A. 2020, *ApJ*, 897, 114, doi: [10.3847/1538-4357/ab9638](https://doi.org/10.3847/1538-4357/ab9638)
- Bradley, L., Sipőcz, B., Robitaille, T., et al. 2022, *astropy/photutils: 1.5.0*, 1.5.0, Zenodo, doi: [10.5281/zenodo.6825092](https://doi.org/10.5281/zenodo.6825092)
- Brown, T. M., Baliber, N., Bianco, F. B., et al. 2013, *PASP*, 125, 1031, doi: [10.1086/673168](https://doi.org/10.1086/673168)
- Chen, T. W., Smartt, S. J., Jerkstrand, A., et al. 2015, *MNRAS*, 452, 1567, doi: [10.1093/mnras/stv1360](https://doi.org/10.1093/mnras/stv1360)
- Chen, Z. H., Yan, L., Kangas, T., et al. 2023, *ApJ*, 943, 41, doi: [10.3847/1538-4357/aca161](https://doi.org/10.3847/1538-4357/aca161)
- Chomiuk, L., Chornock, R., Soderberg, A. M., et al. 2011, *ApJ*, 743, 114, doi: [10.1088/0004-637X/743/2/114](https://doi.org/10.1088/0004-637X/743/2/114)
- Cleland, C., McGee, S. L., & Nicholl, M. 2023, *MNRAS*, 524, 3559, doi: [10.1093/mnras/stad2118](https://doi.org/10.1093/mnras/stad2118)
- Fabricant, D., Fata, R., Epps, H., et al. 2019, *PASP*, 131, 075004, doi: [10.1088/1538-3873/ab1d78](https://doi.org/10.1088/1538-3873/ab1d78)
- Filippenko, A. V. 1982, *PASP*, 94, 715, doi: [10.1086/131052](https://doi.org/10.1086/131052)
- Fitzpatrick, E. L. 1999, *PASP*, 111, 63, doi: [10.1086/316293](https://doi.org/10.1086/316293)
- Flewelling, H. 2018, in *American Astronomical Society Meeting Abstracts*, Vol. 231, American Astronomical Society Meeting Abstracts #231, 436.01
- Förster, F., Cabrera-Vives, G., Castillo-Navarrete, E., et al. 2021, *AJ*, 161, 242, doi: [10.3847/1538-3881/abe9bc](https://doi.org/10.3847/1538-3881/abe9bc)
- Fremling, C. 2024, *Transient Name Server Discovery Report*, 2024-168, 1
- Frohmaier, C., Angus, C. R., Vincenzi, M., et al. 2021, *MNRAS*, 500, 5142, doi: [10.1093/mnras/staa3607](https://doi.org/10.1093/mnras/staa3607)
- Gal-Yam, A. 2012, *Science*, 337, 927, doi: [10.1126/science.1203601](https://doi.org/10.1126/science.1203601)
- . 2019a, *ARA&A*, 57, 305, doi: [10.1146/annurev-astro-081817-051819](https://doi.org/10.1146/annurev-astro-081817-051819)
- . 2019b, *ApJ*, 882, 102, doi: [10.3847/1538-4357/ab2f79](https://doi.org/10.3847/1538-4357/ab2f79)
- Gal-Yam, A., Mazzali, P., Ofek, E. O., et al. 2009, *Nature*, 462, 624, doi: [10.1038/nature08579](https://doi.org/10.1038/nature08579)
- Gerardy, C. L., Fesen, R. A., Marion, G. H., et al. 2002, in *American Astronomical Society Meeting Abstracts*, Vol. 200, American Astronomical Society Meeting Abstracts #200, 14.04
- Gomez, S., Berger, E., Nicholl, M., Blanchard, P. K., & Hosseinzadeh, G. 2022, *ApJ*, 941, 107, doi: [10.3847/1538-4357/ac9842](https://doi.org/10.3847/1538-4357/ac9842)
- Gomez, S., Nicholl, M., Berger, E., et al. 2024, *MNRAS*, 535, 471, doi: [10.1093/mnras/stae2270](https://doi.org/10.1093/mnras/stae2270)
- Guillochon, J., Nicholl, M., Villar, V. A., et al. 2017, *MOSFiT: Modular Open-Source Fitter for Transients*, Astrophysics Source Code Library, record ascl:1710.006
- Hachinger, S., Mazzali, P. A., Taubenberger, S., et al. 2012, *MNRAS*, 422, 70, doi: [10.1111/j.1365-2966.2012.20464.x](https://doi.org/10.1111/j.1365-2966.2012.20464.x)

- Holmbo, S., Stritzinger, M. D., Karamahmetoglu, E., et al. 2023, *A&A*, 675, A83, doi: [10.1051/0004-6361/202245334](https://doi.org/10.1051/0004-6361/202245334)
- Howell, D. A., & Global Supernova Project. 2017a, in American Astronomical Society Meeting Abstracts, Vol. 230, American Astronomical Society Meeting Abstracts #230, 318.03
- Howell, D. A., & Global Supernova Project. 2017b, in American Astronomical Society Meeting Abstracts, Vol. 230, American Astronomical Society Meeting Abstracts #230, 318.03
- Kasen, D., & Bildsten, L. 2010, *ApJ*, 717, 245, doi: [10.1088/0004-637X/717/1/245](https://doi.org/10.1088/0004-637X/717/1/245)
- Kerzendorf, W., Sim, S., Vogl, C., et al. 2024, *tardis-sn/tardis: TARDIS v2024.10.14*, release-2024.10.14, Zenodo, doi: [10.5281/zenodo.13929578](https://doi.org/10.5281/zenodo.13929578)
- Kerzendorf, W. E., & Sim, S. A. 2014, *MNRAS*, 440, 387, doi: [10.1093/mnras/stu055](https://doi.org/10.1093/mnras/stu055)
- Kobulnicky, H. A., Kennicutt, Robert C., J., & Pizagno, J. L. 1999, *ApJ*, 514, 544, doi: [10.1086/306987](https://doi.org/10.1086/306987)
- Lunnan, R., Chornock, R., Berger, E., et al. 2014, *ApJ*, 787, 138, doi: [10.1088/0004-637X/787/2/138](https://doi.org/10.1088/0004-637X/787/2/138)
- Matheson, T., Filippenko, A. V., Li, W., Leonard, D. C., & Shields, J. C. 2001, *AJ*, 121, 1648, doi: [10.1086/319390](https://doi.org/10.1086/319390)
- Mazzali, P. A., Sullivan, M., Pian, E., Greiner, J., & Kann, D. A. 2016, *MNRAS*, 458, 3455, doi: [10.1093/mnras/stw512](https://doi.org/10.1093/mnras/stw512)
- Nagao, T., Maiolino, R., & Marconi, A. 2006, *A&A*, 459, 85, doi: [10.1051/0004-6361:20065216](https://doi.org/10.1051/0004-6361:20065216)
- Nicholl, M. 2021, *Astronomy and Geophysics*, 62, 5.34, doi: [10.1093/astrogeo/atab092](https://doi.org/10.1093/astrogeo/atab092)
- Nicholl, M., Guillochon, J., & Berger, E. 2017, *ApJ*, 850, 55, doi: [10.3847/1538-4357/aa9334](https://doi.org/10.3847/1538-4357/aa9334)
- Nicholl, M., & Smartt, S. J. 2016, *MNRAS*, 457, L79, doi: [10.1093/mnrasl/slv210](https://doi.org/10.1093/mnrasl/slv210)
- Oke, J. B., Cohen, J. G., Carr, M., et al. 1995, *PASP*, 107, 375, doi: [10.1086/133562](https://doi.org/10.1086/133562)
- Oliphant, T. E. 2015, USA: CreateS-pace Independent Publishing Platform
- Pagel, B. E. J., Edmunds, M. G., Blackwell, D. E., Chun, M. S., & Smith, G. 1979, *MNRAS*, 189, 95, doi: [10.1093/mnras/189.1.95](https://doi.org/10.1093/mnras/189.1.95)
- Perley, D. A. 2019, *PASP*, 131, 084503, doi: [10.1088/1538-3873/ab215d](https://doi.org/10.1088/1538-3873/ab215d)
- Perley, D. A., Quimby, R. M., Yan, L., et al. 2016, *ApJ*, 830, 13, doi: [10.3847/0004-637X/830/1/13](https://doi.org/10.3847/0004-637X/830/1/13)
- Planck Collaboration, Aghanim, N., Akrami, Y., et al. 2020, *A&A*, 641, A6, doi: [10.1051/0004-6361/201833910](https://doi.org/10.1051/0004-6361/201833910)
- Prochaska, J. X., Hennawi, J. F., Westfall, K. B., et al. 2020, *Journal of Open Source Software*, 5, 2308, doi: [10.21105/joss.02308](https://doi.org/10.21105/joss.02308)
- Prochaska, J. X., Hennawi, J., Cooke, R., et al. 2020, *pypeit/PypeIt: Release 1.0.0, v1.0.0*, Zenodo, doi: [10.5281/zenodo.3743493](https://doi.org/10.5281/zenodo.3743493)
- Pursiainen, M., Leloudas, G., Paraskeva, E., et al. 2022, *A&A*, 666, A30, doi: [10.1051/0004-6361/202243256](https://doi.org/10.1051/0004-6361/202243256)
- Quimby, R. M., Aldering, G., Wheeler, J. C., et al. 2007, *ApJL*, 668, L99, doi: [10.1086/522862](https://doi.org/10.1086/522862)
- Quimby, R. M., Yuan, F., Akerlof, C., & Wheeler, J. C. 2013, *MNRAS*, 431, 912, doi: [10.1093/mnras/stt213](https://doi.org/10.1093/mnras/stt213)
- Quimby, R. M., Kulkarni, S. R., Kasliwal, M. M., et al. 2011, *Nature*, 474, 487, doi: [10.1038/nature10095](https://doi.org/10.1038/nature10095)
- Roming, P. W. A., Kennedy, T. E., Mason, K. O., et al. 2005, *SSRv*, 120, 95, doi: [10.1007/s11214-005-5095-4](https://doi.org/10.1007/s11214-005-5095-4)
- Schlafly, E. F., & Finkbeiner, D. P. 2011, *ApJ*, 737, 103, doi: [10.1088/0004-637X/737/2/103](https://doi.org/10.1088/0004-637X/737/2/103)
- Schulze, S., Fransson, C., Kozyreva, A., et al. 2024, *A&A*, 683, A223, doi: [10.1051/0004-6361/202346855](https://doi.org/10.1051/0004-6361/202346855)
- Science Software Branch at STScI. 2012, PyRAF: Python alternative for IRAF, Astrophysics Source Code Library, record ascl:1207.011
- Shahbandeh, M., Hsiao, E. Y., Ashall, C., et al. 2022, *ApJ*, 925, 175, doi: [10.3847/1538-4357/ac4030](https://doi.org/10.3847/1538-4357/ac4030)
- Shingles, L., Smith, K. W., Young, D. R., et al. 2021, *Transient Name Server AstroNote*, 7, 1
- Smith, M., Sullivan, M., Nichol, R. C., et al. 2018, *ApJ*, 854, 37, doi: [10.3847/1538-4357/aaa126](https://doi.org/10.3847/1538-4357/aaa126)
- Stevenson, K. B., Bean, J. L., Seifahrt, A., et al. 2016, *ApJ*, 817, 141, doi: [10.3847/0004-637X/817/2/141](https://doi.org/10.3847/0004-637X/817/2/141)
- Sukhbold, T., & Woosley, S. E. 2016, *ApJL*, 820, L38, doi: [10.3847/2041-8205/820/2/L38](https://doi.org/10.3847/2041-8205/820/2/L38)
- Teffs, J., Ertl, T., Mazzali, P., Hachinger, S., & Janka, H. T. 2020, *MNRAS*, 499, 730, doi: [10.1093/mnras/staa2549](https://doi.org/10.1093/mnras/staa2549)
- Valenti, S., Sand, D., Pastorello, A., et al. 2014, *MNRAS*, 438, L101, doi: [10.1093/mnrasl/slt171](https://doi.org/10.1093/mnrasl/slt171)
- Valenti, S., Howell, D. A., Stritzinger, M. D., et al. 2016, *MNRAS*, 459, 3939, doi: [10.1093/mnras/stw870](https://doi.org/10.1093/mnras/stw870)
- Virtanen, P., Gommers, R., Oliphant, T. E., et al. 2020, *Nature Methods*, 17, 261, doi: [10.1038/s41592-019-0686-2](https://doi.org/10.1038/s41592-019-0686-2)
- Williamson, M., Kerzendorf, W., & Modjaz, M. 2021, *ApJ*, 908, 150, doi: [10.3847/1538-4357/abd244](https://doi.org/10.3847/1538-4357/abd244)
- Wise, J., Brennan, S., Sollerman, J., Schulze, S., & Perley, D. 2024, *Transient Name Server Classification Report*, 2024-619, 1
- Woosley, S. E. 2010, *ApJL*, 719, L204, doi: [10.1088/2041-8205/719/2/L204](https://doi.org/10.1088/2041-8205/719/2/L204)
- Yan, L., Perley, D. A., Schulze, S., et al. 2020, *ApJL*, 902, L8, doi: [10.3847/2041-8213/abb8c5](https://doi.org/10.3847/2041-8213/abb8c5)
- Zackay, B., Ofek, E. O., & Gal-Yam, A. 2016, *ApJ*, 830, 27, doi: [10.3847/0004-637X/830/1/27](https://doi.org/10.3847/0004-637X/830/1/27)

Zhu, J., Jiang, N., Dong, S., et al. 2023, ApJ, 949, 23,
doi: [10.3847/1538-4357/acc2c3](https://doi.org/10.3847/1538-4357/acc2c3)